



ORIGINAL RESEARCH ARTICLE

Corrosion Behavior of Ni-Nb Eutectic Glassy Composition in Aqueous Solutions of NaOH, HCl, and NaCl

A.G. Soriano Carranza, I.A. Figueroa, A. Espinoza Vázquez, F.J. Rodríguez Gómez, and L. Huerta

Submitted: 6 March 2022 / Revised: 22 January 2024 / Accepted: 7 February 2024

EIS and cyclic polarization curves in HCl 1 M, NaOH 1 M and NaCl 0.5 M were used to analyze the corrosion mechanism in eutectic Ni-Nb metallic glass composition. Glassy ribbons were synthesized by melt spinning technique by varying the wheel spinning speed with 12 and 25 m/s to produce ribbons of two thicknesses. The vitrification of the alloy was confirmed by XRD, which showed a diffuse characteristic peak of glassy structures. The analyses showed that at pH 0 and 7, the glassy alloy is immune to pitting in its passive layer. Furthermore, it shows regeneration of the damaged areas, repairing those where nickel is lost with niobium oxide. In alkaline media, the passive layer is unstable due to the formation of oxides, increasing the corrosion rate by 0.02 mpy compared to chloride media. When exposed to chloride media and sodium hydroxide, SEM analysis showed no significant damage to the alloy. Finally, XPS was used to analyze the species formed on the surface. Several Ni and Nb oxides were found along different pHs; those species allowed localized corrosion protection, regenerating the damaged zones and corroborating the passive layer's self-healing effect. This effect and the lack of crystalline defects provide high anticorrosion protection of the material.

Keywords corrosion resistance, metallic glasses, Ni-Nb alloy, XPS

1. Introduction

Metallic glasses have short-range structures and excellent mechanical, magnetic, and chemical properties (Ref 1, 2). Furthermore, the literature has reported that amorphous atomic configuration gives them their unique thermo-mechanical properties (Ref 3). Finally, it is worth mentioning that metallic glasses have various applications, among which bioimplants stand out (Ref 4). The study of metallic glasses has been used for proton exchange membrane fuel cells in acid solution (H₂SO₄) (Ref 5) or coating of stainless steel using NaCl (Ref 6).

On the other hand, amorphous metallic glasses used for bioimplants have established themselves as an alternative to traditional implants, as the devices are safer and more effective thanks to the contributions of bioengineering (Ref 7).

In addition, the anticorrosion properties of metallic glasses have been extensively studied since the discovery of highly corrosion-resistant iron-chromium (Fe-Cr) glasses in the 1970s (Ref 8, 9). Metallic glasses can be obtained from molten alloys that are cooled at very high rates so they do not have time to crystallize and acquire a characteristic glassy atomic structure, which is attributed to an excellent high corrosion resistance. On the other hand, the amorphous nickel-based metal has high thermal stability, good mechanical properties and high corrosion resistance (Ref 10). Due to their high temperature and corrosion resistance, Ni-Nb alloys are widely used as coatings in nuclear reactors (Ref 11). Besides, their properties are helping to expand their application in microelectromechanical systems (MEMS) (Ref 12) and structural devices such as gears for micromotors (Ref 13).

Furthermore, the Ni-Nb binary metal system has a good glass-forming ability (GFA) (Ref 14); therefore, it is possible to obtain glassy ribbons from the melt in a wide range of concentrations (Ref 15, 16). Previous studies have shown that the Ni-Nb alloy can form a complete bulk metallic glass (BMG) with a critical diameter of millimeters (Ref 17). Therefore, in the eutectic composition, further vitrification of the alloy is ensured by avoiding the formation of secondary phases.

The mechanical and anticorrosion (in HCl) properties of hypoeutectic Ni-Nb glassy alloys have been reported (Ref 14, 18). However, high corrosion resistance and good mechanical formability of metallic glasses are often found close to eutectics compositions (Ref 19). The Ni₅₀Nb₅₀ systems have been studied by comparing their anticorrosive behavior with their crystalline counterparts (Ref 18). The Ni-Nb system has also been studied as a coating for stainless steels in HCl media (Ref 19). Therefore, this work aims to study the effect of the corrosive medium on the corrosion rate using electrochemical techniques of the Ni_{59.5}Nb_{40.5} glassy alloy and the influence of

A.G. Soriano Carranza, I.A. Figueroa, and L. Huerta, Instituto de Investigaciones en Materiales, Universidad Nacional Autónoma de México, Circuito Exterior S/N, Cd. Universitaria, Coyoacán, 04510 Mexico City, Mexico; A. Espinoza Vázquez, Instituto de Investigaciones en Materiales, Universidad Nacional Autónoma de México, Circuito Exterior S/N, Cd. Universitaria, Coyoacán, 04510 Mexico City, Mexico; and Unidad Anticorrosión, Instituto de Ingeniería, Universidad Veracruzana, 94292 Boca del Río, Veracruz, Mexico; F.J. Rodríguez Gómez, Departamento de Ingeniería Metalúrgica, Facultad de Química, Universidad Nacional Autónoma de México, 04510 Mexico City, Mexico. Contact e-mails: iafigueroa@unam.mx and araespinoza@uv.mx.

the ribbon thicknesses. The alloy behavior to homogeneous and localized corrosion using EIS was also assessed.

2. Materials and Methods

An argon arc furnace was used to prepare the Ni-Nb alloy ingots. First, the furnace was evacuated to a pressure of 2×10^{-5} torr, using a rotary and diffusion pump system. Then, the furnace was filled with 1/4 atmosphere of argon. A Ti button was used to remove residual oxygen before melting the alloy sample. The sample was turned over and remelted at least five times to ensure homogeneity. The alloy ingots were broken into smaller pieces and placed in a quartz crucible with a nozzle diameter of 0.8 mm. The melt spinning chamber was evacuated to 9×10^{-3} torr and then filled with 4/5 atm of helium. The alloy was melted by radio frequency and induction heating. The molten metal was ejected using an argon ejection pressure of 0.3 bar on the rapidly rotating copper wheel. Two tangential wheel speeds were used, 12 and 25 m/s, to produce ribbons of two thicknesses. The structural characterization was performed using x-ray diffraction analysis on a Siemens D5000 diffractometer. The ribbons were glued to a flat surface to ensure compliance with Bragg's law. The study was performed with Cu lamp radiation and a scanning range of 30 to 100 degrees.

For the electrochemical evaluation by EIS and CP, the working electrode was the glassy alloy (previously cleaned with acetone in an ultrasonic device) with an exposed area of 10×2.5 mm, exposed on one side (25 mm^2). A graphite rod acted as a counter electrode, and saturated Ag/AgCl was used as the reference electrode. The experiments were performed at different pH, i.e., 0, 7 and 14 at room temperature with HCl 1 M, NaOH 1 M (Meyer, purity > 97.9 %) and NaCl 0.5 M (Meyer, purity > 99%). The 3-electrode array was connected to a Gill AC galvanostatic potentiostat by performing the following test sequence: (1) OCP for 1800 s at one count per second, (2) impedance with an AC frequency of 10 KHz at 0.01 Hz, with a wave perturbation of 10 mV and (3) cyclic polarization curves were obtained with a sweep of 1 mV/s from cathodic to anodic; the reversal potential in anodic branch was 1 V versus the rest potential. Tests were performed in triplicate for statistical purposes. Regarding the effect of immersion time, once the corrosive medium to which the ribbons showed the best corrosion protection was determined, a follow-up EIS was performed using the same electrochemical arrangement at different immersion times (360 h).

The surface characterization through SEM-EDS of the Ni-Nb ribbons was performed before and after the continuous immersion in each studied corrosive solution studied for 24 h. After the experiment, the ribbons were cleaned with distilled water and dried with absorbent paper. The surface was analyzed by scanning electron microscopy, using a Jeol-JBM-7600F microscope at 10 kV, with a secondary electron detector at different magnifications.

The x-ray photoelectron spectroscopy (XPS) measurements were performed on Versa Probe II equipment, which has a monochromatic x-ray source of Al K_{α} ($h\nu = 1486.6 \text{ eV}$) with $100 \mu\text{m}$ of the beam diameter. The sample surfaces were etched with Ar^+ at 3 kV and $0.25 \mu\text{A}$ for 1 minute. The measurements were carried out at 45° with respect to the surface and with a Constant Analyzer Energy (CAE) of 10 eV for the high-resolution spectra. The analysis of the spectra and the

deconvolutions were carried out with the SDP V4.1 program. X-ray photoelectron spectroscopy analyses were performed in an ultra-high vacuum (UHV) system Scanning XPS microprobe PHI 5000 VersaProbe II, with an Al K_{α} x-ray source ($h\nu = 1486.6 \text{ eV}$) monochromatic with $100 \mu\text{m}$ beam diameter, and an MCD analyzer. The XPS spectra were obtained in the constant analyzer energy (CAE) $E_0 = 117.40$ and 11.75 eV survey surface and high-resolution narrow scan. The surface samples were etched for 4 min with 1 kV Ar^+ at $1 \mu\text{A}/\text{mm}^2$. Peak positions were referenced to the background silver $3d_{5/2}$ photopeak at $368:20 \text{ eV}$, having an FWHM of 0.56 eV , and C $1s$ hydrocarbon groups at $285:00 \text{ eV}$, Au $4f_{7/2}$ in 84.00 eV central peak core level position and corrected by MultiPak PHI software. The XPS analysis deconvolution of spectra was fitted with SDP v 4.1 program. The deviation of binding energy for the central peak estimated the uncertainty of about 5% ($\pm 0.05 \text{ eV}$) and a chi-square value of less than 1.0 in deconvolution analysis.

3. Results and Discussion

3.1 Characterization by Means of XRD

Figure 1 shows the diffraction pattern of the alloys, showing the diffuse peaks, being the main characteristic of glassy alloys, indicating a short-range atomic arrangement (Ref 18). The wheel spinning speed does not significantly affect the vitrification of the ribbons for this composition, but it does affect the surface quality.

3.2 Open-Circuit Potential (OCP)

Figure 2 shows the OCP test. It is observed that the system stabilizes its potential at around 1000 sec, having more activity in the basic medium. It should be noted that all the potential values increase as a function of time, having a more noble or protective behavior of the species formed on the surface, suggesting the formation and growth of the passive layer.

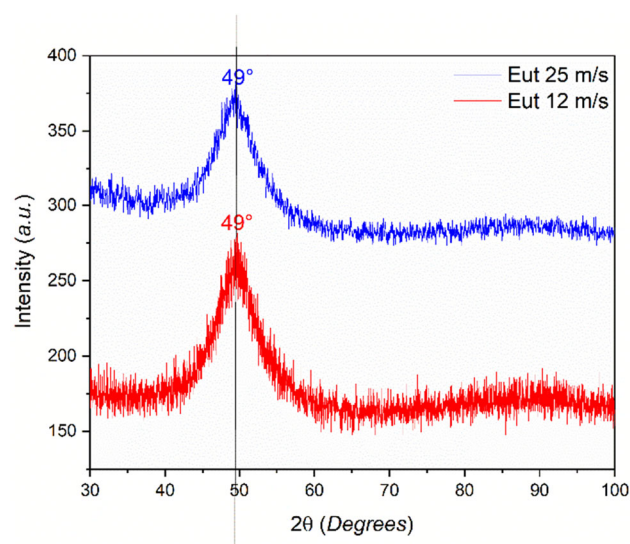


Fig. 1 X-ray diffractogram for Ni-Nb metallic glass ribbons for the eutectic composition cast at 12 and 25 m/s

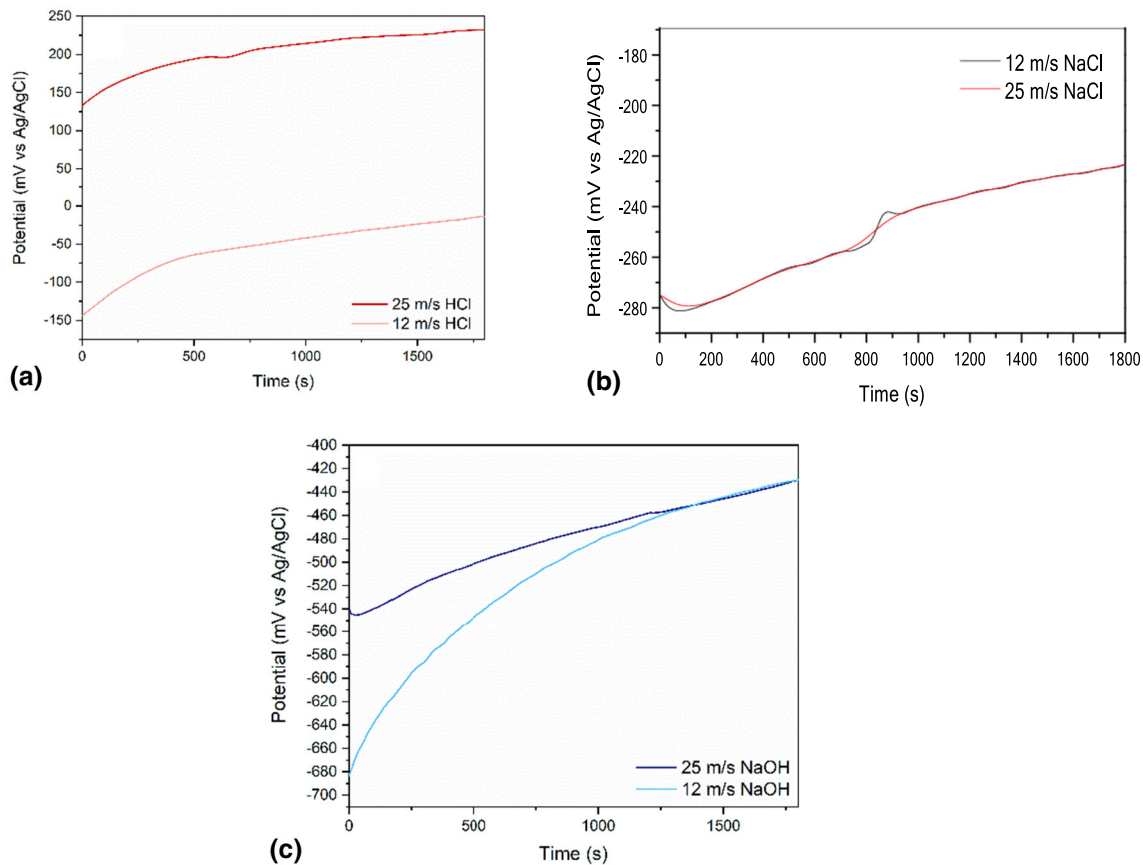


Fig. 2 Open-circuit potential of the Ni-Nb ribbons immersed in different corrosive media: (a) HCl, (b) NaCl and (c) NaOH

3.3 Effect of pH Through EIS

Figure 3 shows the Nyquist diagram for the samples immersed in (a) HCl, (b) NaCl and (c) NaOH, showing a highly resistive and capacitive behavior; the semicircle shape is similar for both cooling rates. Figure 3(b) shows the results obtained for the sample produced with both wheel speeds immersed in NaCl. However, the sample cast at 12 m/s has a lower R_{ct} value of $1.84 \times 10^6 \Omega \text{ cm}^2$ than the other velocity, which is lower in both impedance components. For NaOH (Fig. 3c), the R_{ct} value decreases in one order magnitude than for the chloride media (HCl and NaCl) at 12 m/s (see Table 1), while the highest R_{ct} value obtained was $5.55 \times 10^5 \Omega \text{ cm}^2$ for the 25 m/s cast sample.

On the other hand, Z_{real} was one order of magnitude lower. This medium is, therefore, the most corrosive for the Ni-Nb vitreous alloy studied. Finally, the results showed that the 12 m/s cast sample constantly presented a lower R_{ct} value for any studied corrosive media (Fig. 3a-c). This was attributed to the fact that this vitreous alloy showed a different surface morphology, i.e., more superficial defects were observed, affecting its corrosion resistance.

Figure 4 shows the equivalent electrical circuit used to make the adjustments. The model used three resistors: the solution resistance (R_s), the passive film resistance (R_{po}) and the charge transfer resistance (R_{ct}) and two elements of constant phase (Q_1 and Q_2) in parallel fits the physical model of a coating with porosities since at immersion time 0 it is assumed that the material has a porous passive layer.

The double layer capacitance (C_{dl}) was calculated by (Ref 20):

$$C_{dl} = Y_0^{\frac{1}{n}} \left[\left(\frac{1}{R_s} \right) + \left(\frac{1}{R_{ct}} \right) \right]^{\frac{n-1}{n}} \quad (\text{Eq 1})$$

where Y_0 is a proportion factor. n is the phase change, which can take values of 0 for a resistance, 1 for a capacitance and -1 for an inductance.

The electrochemical parameters obtained by adjusting the electrical circuit of Fig. 4 are shown in Table 1. When analyzing the R_{ct} , the lowest value was found for the 12 m/s sample and the highest for the 25 m/s. Therefore, this work presents a comparative graph for the media used with the best results. Figure 5 shows the Nyquist plots at 25 m/s, where the material is more susceptible to the corrosion process at pH = 14. However, it is important to underline that, despite the extreme conditions (high chloride content), this kind of alloy is very corrosion-resistant at pH = 0 and 7.

It was also observed that the wheel speed of the melt spinner influences the electrochemical properties of this material, with the best conditions being observed for the 25 m/s sample. This could be attributed to the different surface conditions due to the wheel speed and the interaction between the molten metal and the cooper wheel surface, suggesting a rougher surface at the lowest wheel speeds. These phenomena can be observed using EIS, as this technique has the sensitivity to detect electrode surface differences less than a one-micron scale. Likewise, the corrosion products modified the surface structure in contact

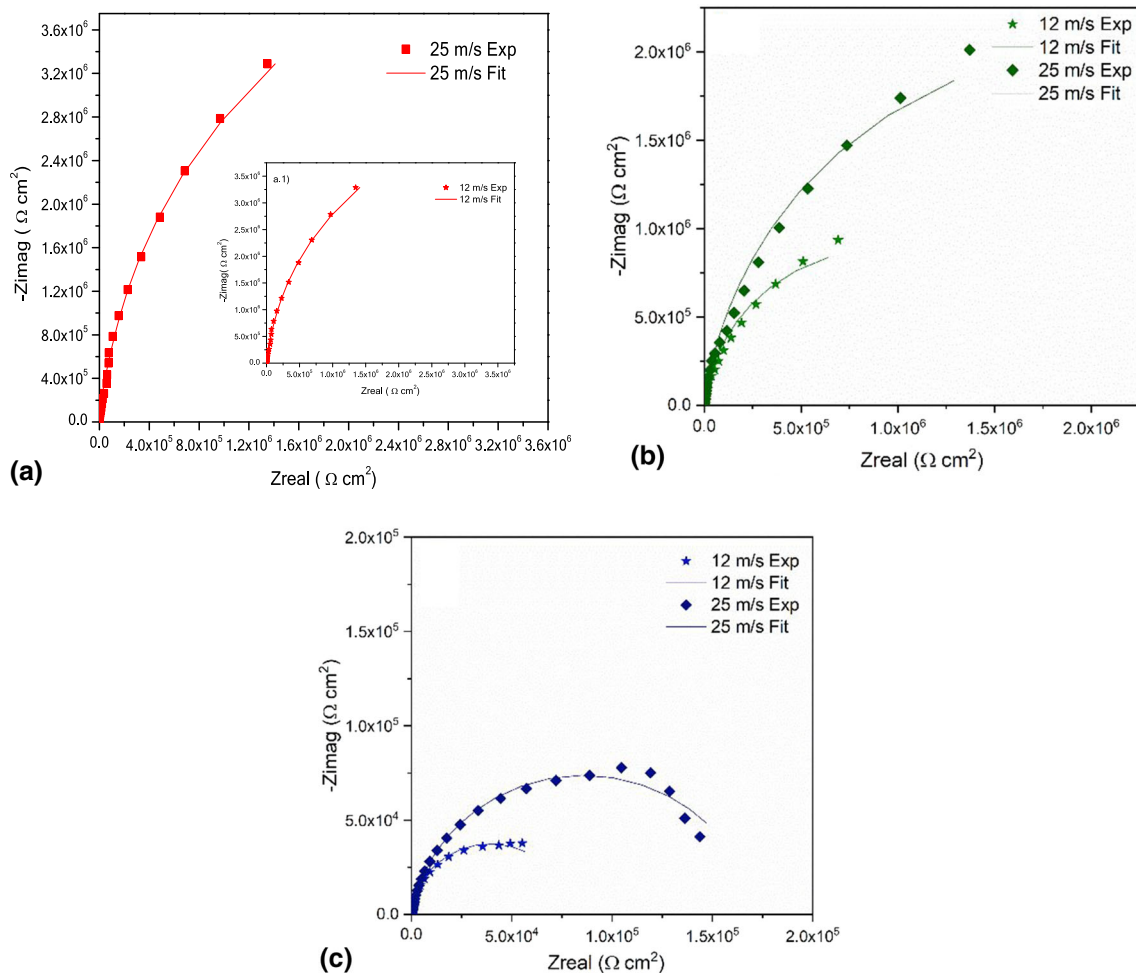


Fig. 3 Nyquist diagram of the Ni-Nb metallic glass at different wheel spin velocities immersed in (a) HCl, (b) NaCl and (c) NaOH

Table 1 Obtained electrochemical parameters at different corrosive media for wheel speeds of 12 and 25 m/s

V , m/s	Medium	R_s , $\Omega \text{ cm}^2$	C_{po} , $\mu\text{F}/\text{cm}^2$	n	R_{po} , $\Omega \text{ cm}^2$	C_{dl} , $\mu\text{F}/\text{cm}^2$	R_{ct} , $\Omega \text{ cm}^2$	SD (\pm)
12	HCl	1.8	1.0	0.97	1.28×10^6	1.8	1.97×10^6	1.85
	NaCl	15.5	1.1	0.95	1.05×10^6	1.1	1.84×10^6	3.36
	NaOH	9.5	4.9	0.96	7.86×10^4	2.0	1.65×10^4	0.39
25	HCl	4.2	2.5	0.93	2.49×10^6	4.2	2.70×10^6	0.15
	NaCl	24.9	2.6	0.91	2.70×10^6	4.4	2.64×10^6	3.04
	NaOH	14.6	3.1	0.96	6.19×10^4	5.7	1.55×10^5	3.58

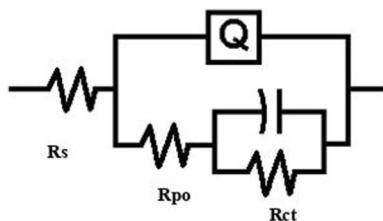


Fig. 4 Equivalent electric circuit used in the simulation of experimental data

with the solution, creating a physical barrier that does not allow corrosive ions (chlorides or oxygen) to diffuse into the material (Ref 21).

Therefore, this work presents a comparative graph for the media used with the best results. Figure 5 shows the Nyquist plots at 25 m/s, where the material is more susceptible to the corrosion process at pH = 14. However, it is important to underline that, despite the extreme conditions (high chloride content), this kind of alloy is very corrosion-resistant at pH = 0 and 7.

The Bode plots are shown in Fig. 6 under different test conditions. The absolute impedance $|Z|$ vs log Freq in Fig. 6(a) shows the same slope with the best corrosion resistance when immersed in 1 M HCl. In Fig. 6(b), the maximum phase angles of all tested ribbons were observed, close to or exceeding 80° , indicating the passive film on the surface of the alloy (Ref 22). This phase angle describes the stability and insulation of the passivation film (Ref 23), while in NaOH media, the drop in the angle at low frequencies would imply instability of the film.

On the other hand, the phase angle shows a broad curve that can be attributed to having two contributions in the intermediate frequency range, which implies the presence of two-time constants: one attributed to the charge transfer resistance and the other to the passive film formed (Ref 24).

According to the system obtained for the NaOH (Table 1), the R_{po} is higher than R_{ct} , and C_{po} is higher than C_{dl} , indicating a higher activity in the coating pores, which might produce

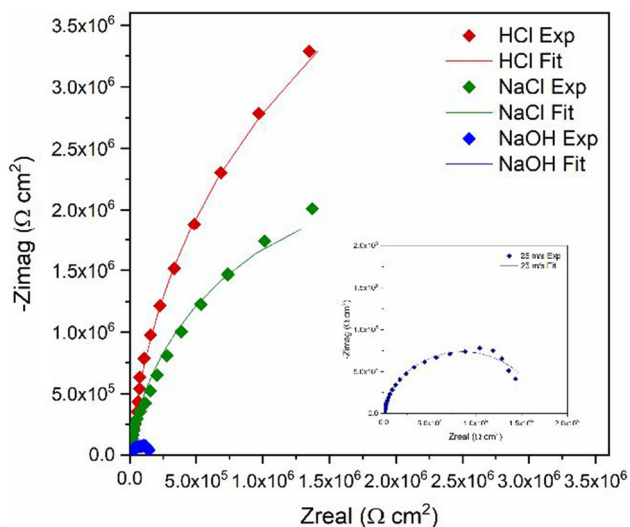
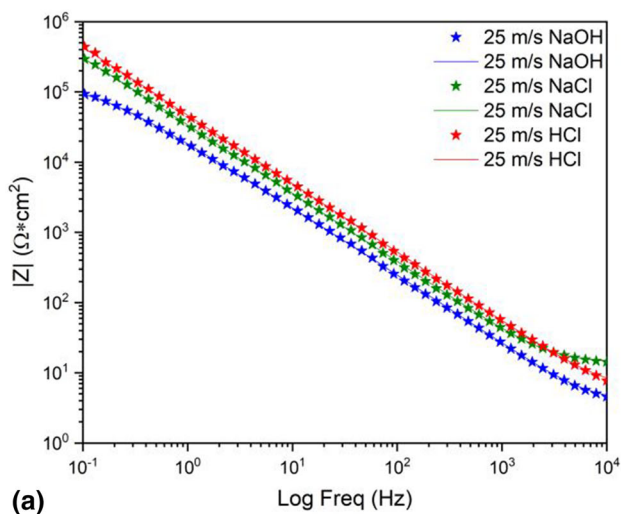


Fig. 5 Nyquist diagram for Ni-Nb metallic glass at a tangential wheel speed of 25 m/s, immersed in different corrosive media



another kind of deposit when the passive layer reacts to the medium. If the passivant species were changed, the R_{ct} would decrease, losing the protective layer.

3.4 Effect of the Corrosive Medium for the Sample Cast at 25 m/s Through Polarization Curves

The behavior of the vitreous material in different media, generated at 25 m/s, can be observed in Fig. 7. For the neutral medium, it presents a potential value closer to that of nickel (-250 mV) (Ref 25); in the acid medium, it is more positive, and in the basic medium, the opposite occurs (more negative potential). It should be noted that the cathodic slopes are the same in acid and neutral pH are the same, but they change in the basic medium as they are more pronounced. On the other hand, in 10^{-6} A/cm², a vertical zone is observed in the three corrosive media, which is associated with passivation. In reverse, when the potential reached 1 V in relation to E_{corr} , only the sample in the NaOH medium reached the breakdown

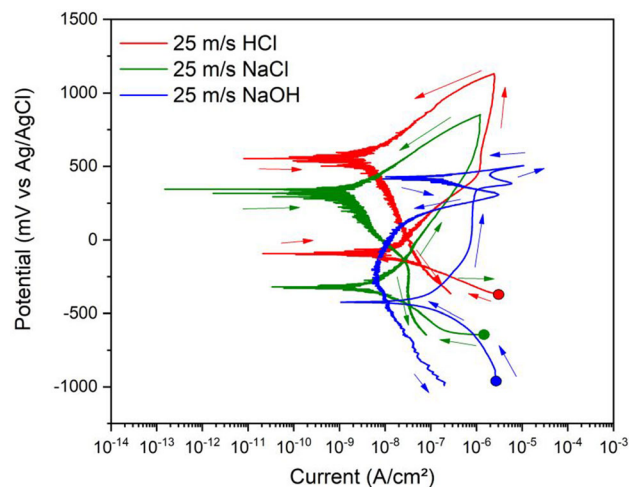


Fig. 7 Cyclic potentiodynamic curve of Ni-Nb metallic glass ribbons cast at 25 m/s and different corrosive media

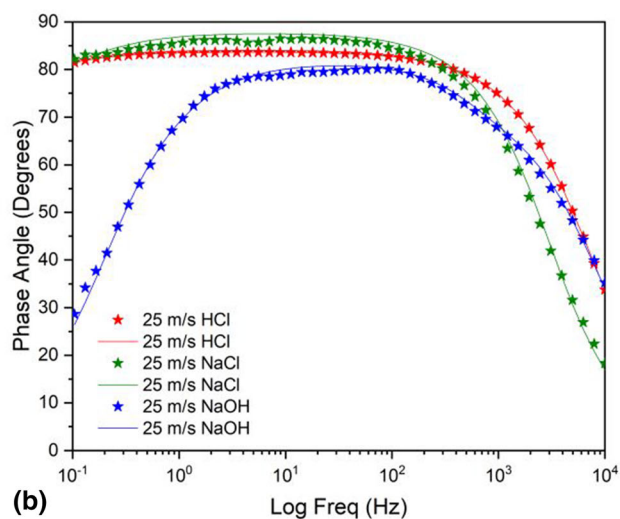


Fig. 6 Bode plots for Ni-Nb metallic glass at a tangential wheel speed of 25 m/s, immersed in different corrosive media

potential. However, it is clear that if the breakdown current density should have had 10^{-3} A/cm², all the samples would have shown the breakdown.

Similar anticorrosive behavior was observed for the media containing chlorides (HCl and NaCl), being slightly lower in the neutral medium than in the acidic one. A negative hysteresis in the cyclic polarization curves means that the corrosion products are more protective than the original material. The same potential value gives lower current values when the polarization is inverted. The polarization curves showed pseudo-passivation, which means that the corrosion products are neither adherent nor homogeneous and therefore have a low protective quality. In this sense, the pseudo-passivation was more clearly observed as the slope changed. This could be associated with a change in the species' oxidation state than a homogenous protective film deposit.

The electrochemical parameters obtained from the polarization curves are given in Table 2, where $\log i_{\text{corr}}$ is the logarithm of the corrosion current density, E_{corr} is the corrosion potential, passivation current (i_{pas}), breakdown potential (E_b), pitting potential (E_{pic}), anodic Tafel slope (ba), cathodic Tafel slope (bc) and corrosion rate (V_{corr}). The results indicate that the Ni-Nb metallic glasses are more corrosion-resistant at pH = 0. However, other studied pHs gave comparable corrosion rates, attributed to their short-range arrangement (fully vitreous structure).

Finally, for the NaOH medium, a vertical zone associated with the material's passivation of the material was observed. It does not show the characteristic current drop of the protective film. It was suggested that the corrosion products were not as protective as expected; after the film break (E_{pic}), a peak of

around 500 mV was observed. This was attributed to the formation of another species, which was dissolved when the potential was inverted. This has been reported as the migration of protective species (Ref 25), confirming a negative hysteresis in the potential inversion. However, it has been reported that the difference between E_{corr} and E_{pic} , the one with the most significant difference, indicates that the passive film is more stable, as is the case of the 12 m/s cast ribbon when immersed in NaOH (Ref 26). It has also been reported that metallic glasses show that the current densities (j) for the samples tested decreased, indicating surface passivation (Ref 27).

It is thought that the products formed in the shape of a film increased the corrosion rate as it was less stable and adherent, or the passive layer of the alloy could react, a phenomenon also seen in the EIS values. Regarding the media with chlorides, a reaction with another species might be produced when the cathodic slope increases. This reaction would create degradation zones of the passive layer, being more susceptible to corrosion, raising it to 0.02 mpy compared to the presence of chlorides (Ref 28). According to the polarization curve, the pitting potential (E_{pic}) is 0.38 V, and the logarithm of the passivation current is between $-2.7y - 2.9$ mA/cm². Once the corrosion rates have been calculated, according to Fontana's criteria (Ref 29), the corrosion rate is outstanding, being lower than one mpy for all the conditions.

3.5 Effect of Immersion Time

Figure 8 shows the Bode plot and R_{ct} variation as a function of immersion time. The Bode diagram of Fig. 8(a) presents the behavior at different immersion times (13 days), immersed in

Table 2 Obtained electrochemical parameters by adjusting the Tafel slopes

V , m/s	Corrosive medium	i_{corr} , $\mu\text{A}/\text{cm}^2$	E_{corr} , mV vs Ag/AgCl sat.	i_{pas} , $\mu\text{A}/\text{cm}^2$	E_b , V	ba , mV/dec	$-bc$, mV/dec	V_{corr} , mpy
12	HCl	1.11	-172.3	1.00	...	326.3	103.5	0.061
	NaCl	1.08	-322.6	1.26	...	360.5	113.1	0.061
	NaOH	1.53	-360.2	2.00	0.34	282.9	166.1	0.085
25	HCl	1.02	-187.2	1.26	...	263.7	115.2	0.058
	NaCl	1.23	-326.8	2.51	...	328.4	117.2	0.069
	NaOH	1.49	-361.5	1.26	0.33	295.8	167.2	0.080

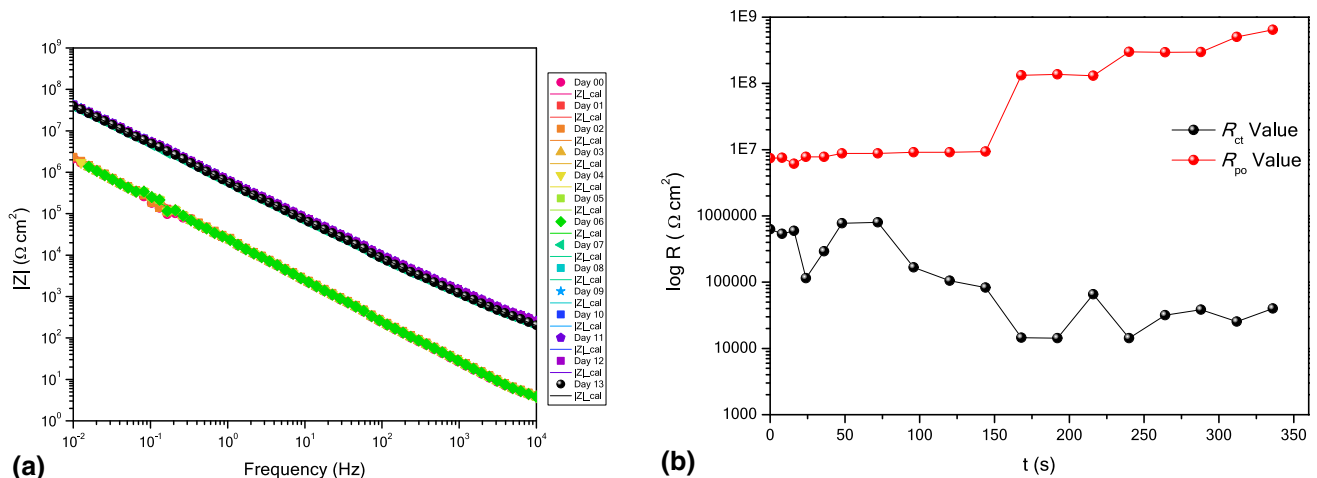


Fig. 8 (a) Bode diagram and (b) resistance variation of Ni-Nb metallic glass ribbons at 25 m/s, immersed in HCl 1 M

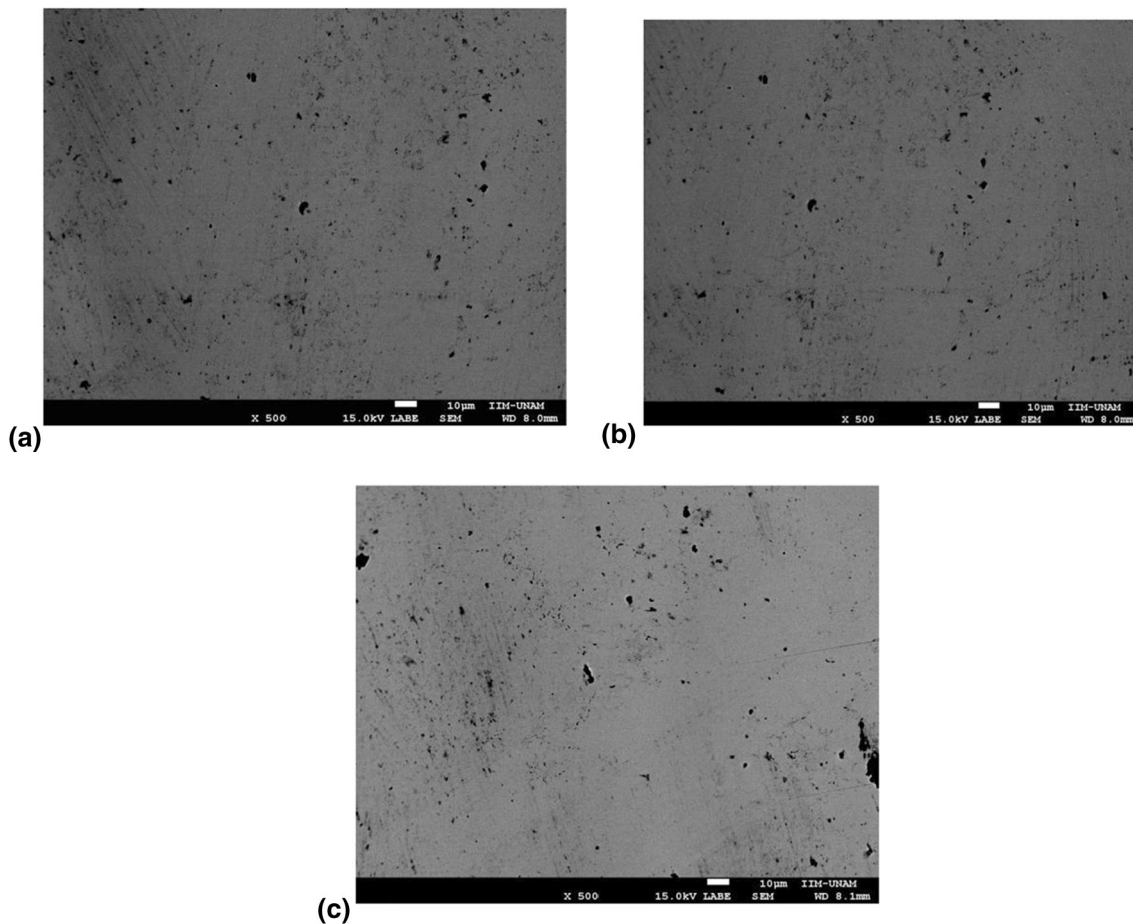


Fig. 9 SEM at 500X for the 12 m/s ribbon (a) in HCl 1 M (b) NaCl 0.5 M and (c) NaOH 1 M before corrosion tests

HCl 1 M. For this system, the $\text{Log}|Z|$ remains practically constant in a lapse of 1 h to 144 h. However, it increases by one order of magnitude at 168 h and rises again at 336 h. The presence of a passive protective film can explain this type of behavior. It is worth noting that this oxide protects the metal because the solution penetrates slowly and does not damage the protective film, making it corrosion-resistant for long immersion times.

The R_{ct} and R_{po} values are shown in Fig. 8(b). During the 336 h of immersion, the R_{po} parameter is higher than the R_{ct} value in the corrosion system. This observation has been attributed to the passive film, which is resistant to an aggressive medium because the pores are sealed over time, making it a more compact film (Ref 30).

3.6 Characterization by Means of SEM-EDS

SEM-EDS images of the Ni-Nb metallic glass under the different conditions studied and the microstructure are shown in Fig. 9 and 10 at 500 X. In the sample cast at 12 m/s sample (Fig. 9a), surface irregularities along the material (produced when cooling down the material) were observed. These surface defects increase the material's porosity, making it susceptible to charge transfer, and lowering the R_{ct} values. The EDS (Fig. 10a) shows a Ni-Nb composition with minimal amounts of oxygen; the presence of this element is associated with passive film formation. Then, Fig. 9(b) presents a gray-colored

homogenous matrix with micrometric black inclusions ($< 10 \mu\text{m}$). However, the EDS analysis showed only the alloying elements Ni-Nb, and the oxygen detected was associated with the passive film to a lesser proportion (Fig. 10b).

However, for the NaCl (Fig. 9b) and NaOH (Fig. 9c) media, the micrographs showed the same vitreous matrix with more black precipitates. Finally, for further clarification of the contribution of ions present in the metallic ribbon in the EDX spectra (Fig. 10), the % atomic of peaks are shown in Table 3. The EDX for these samples (Fig. 10b and c) showed that the corrosive species on the surface of the ribbon are mainly composed of chloride and sodium ions (from the NaCl and NaOH media). Therefore, it is noteworthy that neither pitting on the material's matrix nor holes on the surface, denoting the material's loss, were observed.

The results reported in this work show that the Ni-Nb alloy glasses have high corrosion resistance in the proposed pH analysis. The most remarkable result was obtained for the most aggressive medium analyzed, i.e., for NaOH at a pH of 14, no corrosion products were observed in the glassy alloy surface, even at $15000\times$. According to the observations from the experimental techniques, the material passivation was corroborated, in good agreement with the evolution behavior of the OCP and the characteristic shape of the Nyquist diagrams (capacitive and very resistive). The EIS simulations also confirmed the high resistances and low capacitances associated with a good performance of the protective coating. Further-

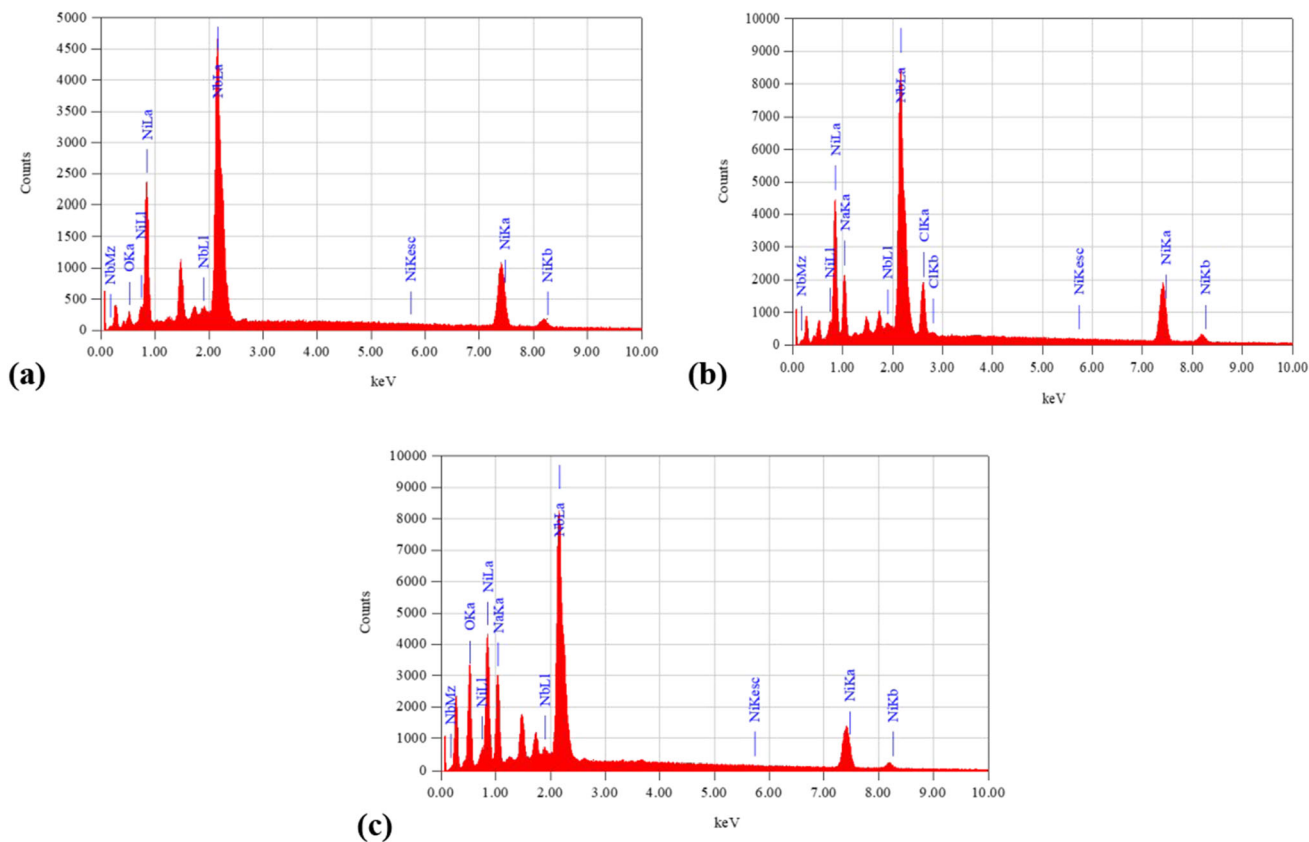


Fig. 10 EDX for the 12 m/s ribbon (a) in HCl 1 M, (b) NaCl 0.5 M and (c) NaOH 1 M before corrosion tests

Table 3 Content of elements obtained from EDX spectra at different conditions

Element	Ribbon	% Atomic		
		Ribbon + HCl	Ribbon + NaCl	Ribbon + NaOH
Nb	40.6	40.69	40.71	39.20
O	2.14	12.95	...	4.3
Ni	57.26	46.36	13.72	53.96
Cl	14.9	...
Na	2.54

more, the SEM micrographs confirmed that the material's surface plays a crucial role in the corrosion resistance of the investigated glassy alloy. The roughest surface was observed on the sample cast at 12 m/s; coincidentally, the corrosion resistance of this sample was the worst. When the material was exposed to a basic medium, the results obtained with the employed electrochemical techniques suggested a further reaction on the coated surface (second passivation).

3.7 Characterization by Means of XPS

The ribbons at 25 m/s samples were analyzed with x-ray photoelectron spectroscopy (XPS); the wide scan spectra are shown in Fig. 11. The samples were etched with Ar ions only for 1 min with 1 kV in $1 \mu\text{A}/\text{mm}^2$ to expose oxides on the passivated surface, and thus a tiny signal of C 1s peak was observed. The C 1s and Nb 3d (of Nb₂O₅) core levels were

used to calibrate the binding energy positions for all oxidation estases observed, as shown in Table 4.

Figure 12(a-g) displays Nb 3d, Ni 2p_{3/2}, and O 1s core levels' high-resolution spectra. Figure 12(a) shows the deconvoluted XPS spectra for 25 m/s ribbon samples in the binding energy (BE) region of Nb 3d_{5/2}; only one peak is observed at BE = 203.32 eV, and 204.10 eV corresponds to Nb and NbO, which is consistent with reported data (Ref 31-33). Nb metal and Nb₂O₅ spectra are also shown as a reference (up shown with a thin line); the Nb metallic compound is present in all samples. Nb 3d core level orbital is shown in Fig. 12(a), (c), (e), and (g), respectively. The deconvolution shows two main contributions corresponding to niobium in Nb and NbO. The sample with NaOH shows other contributions corresponding to Nb₂O₅ and other non-stoichiometric oxides; the contributions were located at BE = 207.60 eV and 205.40 eV, respectively.

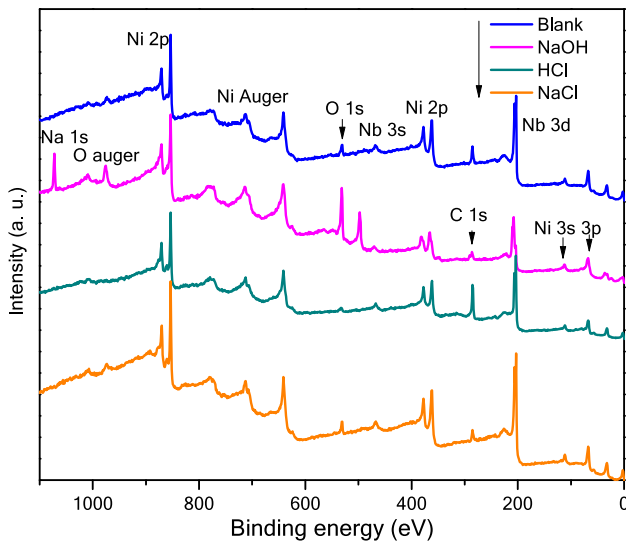


Fig. 11 XPS survey scan spectra of the ribbon cast at 25 m/s: Blank, NaOH, HCl and NaCl samples

Figure 12(b) shows the deconvolution of the Ni $2p_{3/2}$ core level orbital for the 25 m/s sample. The binding energy position is 853.35 eV and 855.45 eV, corresponding to Ni metallic and NiO in agreement with reported values (Ref 34-36); a similar contribution could be observed in Ni $2p_{3/2}$ core level in the other samples, Fig. 12(d), (f) and (h).

Ni $2p_{3/2}$ core level corresponding to Ni and NiO are shown (up thin line) in Fig. 12(b); all analyzed samples present metallic nickel. Only the NaOH sample contains a small amount of Ni_2O_3 . NiO is observed in all samples of the high-resolution spectra.

Nb is more negative than Ni, and therefore, Nb dissolves and oxidizes first. It has been shown that the higher the potential and the more stable the oxide or hydroxide concentration reaches saturation, the more stable the passivation film (Ref 37).

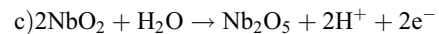
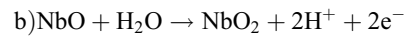
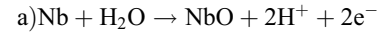


Table 4 XPS results of elemental composition, binding energies at Nb $3d$, Ni $2p$ and O $1s$ core level of the ribbon samples at 25 m/s and the assignment of photoemission signals to corresponding chemical compounds

*% Atomic composition Sample	Nb		Ni		O	Chemical state	Chemical content, %
	$3d_{5/2}$	$3d_{3/2}$	$2p_{3/2}$	$2p_{1/2}$	1s		
	Binding energy, eV						
% Without corrosive media	59.3		19.5		21.3		
	203.32	206.09				Nb	57.3
	204.10	206.87			533.40	NbO	36.5
	205.40	208.17			531.98	NbO _x	6.2
			853.35	870.65		Ni	62.3
			854.54	871.84	530.83	NiO	37.7
			860.25	876.84		**Satellite	
% NaOH	67.8		28.0		3.4		
	203.32	206.09				Nb	18.5
	204.10	206.87			533.39	NbO	12.1
	205.40	208.17			531.98	NbO _x	3.0
	207.60	210.36			530.58	Nb ₂ O ₅	62.6
			854.53	870.63		Ni	53.7
			860.25	871.84	530.97	NiO	33.7
			856.88	877.78		**Satellite	
			853.33	874.18	531.31	Ni ₂ O ₃	12.6
% HCl	55.8		24.4		19.8		
	203.32	206.09				Nb	62.2
	204.10	206.87			533.38	NbO	37.8
			853.38	870.65		Ni	58.5
			854.54	871.84	530.83	NiO	41.5
			860.27	877.57		**Satellite	
% NaCl	61.2		19.9		18.9		
	203.32	206.09				Nb	63.5
	204.10	206.87			533.52	NbO	36.5
			853.35	870.65		Ni	
			854.54	871.84	530.86	NiO	
			860.25	876.84		**Satellite	
Nb ⁰	203.32	206.09				Nb	
Nb ⁵⁺	207.60	210.36			530.58	Nb ₂ O ₅	
Ni ⁰			853.35	870.65		Ni	
Ni ²⁺			855.45	873.88	530.86	NiO	
					532.65	**Satellite	
Ref. C 1s			285.00			C-C	

Atomic sensitivity factor (ASF) quantification used at Ni $2p$ 1.590, Nb $3d$ 9.830 and O $1s$ 0.733 (*), and corresponding to shake-up satellite of Ni $2p$ core level of NiO (**)

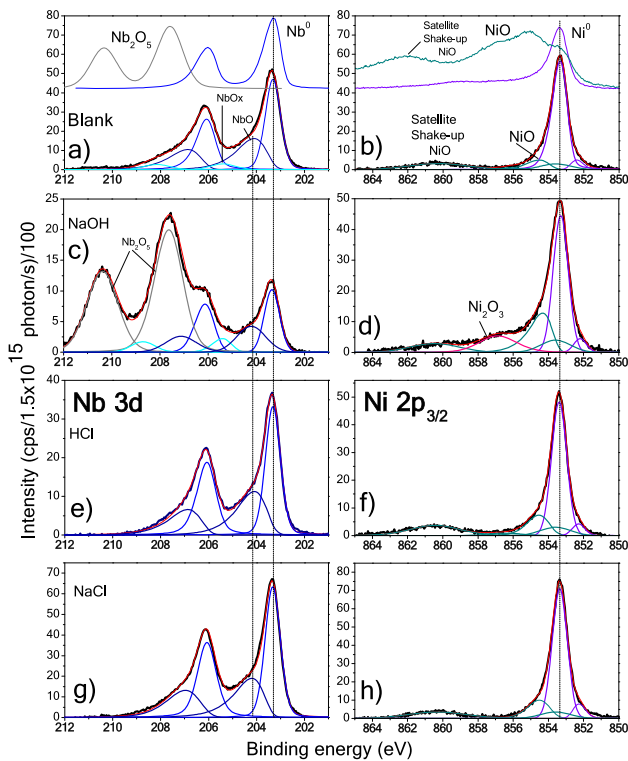


Fig. 12 High-resolution XPS spectra of Nb $3d$, Ni $2p_{3/2}$ and Fe $2p$ core level of the treated MLS. Deconvolution analysis of Nb $3d$ orbital (a) Blank, (c) NaOH, (e) HCl and (g) NaCl; Nb₂O₅ and Nb⁰ are shown as references in (b). The (b, d, f and h) showed deconvolution analysis of Ni $2p_{3/2}$ core level for samples in the same order; NiO and Ni⁰ are shown in (b)

For the NaOH medium, the oxide film formed is Nb₂O₅, which results from the partial oxidation of NbO₂ to Nb₂O₅ by the presence of oxygen (O₂) and hydroxyl groups (OH⁻) (Ref 38, 39).

On the other hand, the metallic glass, when exposed to an acidic medium and, as the solution was not deaerated, in principle, the Nb come in contact with the oxygen in the air, reacting to form ionic bonds of NbO and NiO (Ref 40). Probably, the acidic medium displaces the reactions, preventing the formation of oxides. On the other side, the alkaline medium consumes the hydrogen ions, displacing the reaction to the formation of oxides and hydroxides.

4. Conclusions

The Ni-Nb binary metallic glasses of eutectic composition showed a short-range structure, presenting a fully vitreous phase. The use of electrochemical techniques such as electrochemical impedance spectroscopy and polarization curves allows us to adequately describe the corrosion mechanism of the alloy to different corrosive media. The electrochemical results obtained by EIS showed that the corrosion products also protect at a wheel speed of 25 m/s at pH = 14. On the other hand, it was corroborated that, at this pH, the passive film reacts with the medium, originating a defective interface that increases the corrosion rate by 0.020 mpy, compared to the media with chlorides (NaCl and HCl). Therefore, the wheel speed of 25 m/

s was beneficial to the corrosion resistance of the alloy in the three media.

The Fontana's stability criteria (Ref 29) to measure corrosion resistance was < 1 mpy, indicating that the behavior of the studied alloy is outstanding when immersed in different corrosive media (acid, basic and neutral). The melt spinner wheel speeds affected the surface's homogeneity, causing a rougher surface that increased the corrosion rate. The kinetic effect of 25 m/s ribbons in HCl 1 M showed a compact film and controlled corrosion process during 336 h of immersion, with higher coating resistance values. The SEM micrographs confirmed that the oxide layer on the surface of the alloy was homogeneous. Through XPS, it was found that most alloys have metallic nickel, NiO, Nb metallic, and NbO. Only in pH 14 were other phases identified in a smaller proportion, i.e., Nb₂O₅ and Ni₂O₃.

Finally, with the XPS results, besides the polarization curves, it can be concluded that passivation in the metallic glasses was observed in the three corrosive media studied.

Acknowledgments

AGSC, AEV and FJRG express gratitude to the Facultad de Química (UNAM), Departamento de Ingeniería Metalúrgica. We also wish to acknowledge the SNI (Sistema Nacional de Investigadores) for the distinction of their membership and the stipend received. IAF would like to acknowledge the financial support from DGAPA-PAPIIT UNAM "IN102422" for funding the project. C. Flores, G. A. Lara-Rodriguez, A. Tejada, O. Novelo-Peralta, C. Ramos, R. Reyes, A. Pompa, F. Garcia, E. Hernandez-Mecinas and A. Bobadilla are also acknowledged for their technical support.

Data Availability

The data supporting this study's findings are available from the corresponding author upon reasonable request.

Conflict of interest

The authors declare no financial or commercial conflict of interest.

References

1. A.L. Greer and E. Ma, Bulk Metallic Glasses: At the Cutting Edge of Metals Research, *MRS Bull.*, 2007, **32**(8), p 611–619.
2. N. Wang, Q.P. Cao, W. Yao, X.D. Wang, D.X. Zhang, H.-J. Fecht, and J.Z. Jiang, Anisotropic and Size-Dependent Mechanical Responses of Free-Standing Ni-Nb Metallic Glass Thin Film, *Scr. Mater.*, 2021, **198**, p 113832.
3. A.G. Murphy, P. Meagher, A. Norman, and D.J. Browne, Mechanical and Thermal Stability of Bulk Metallic Glass Alloys Identified as Candidate for Space Mechanism Applications, *Mater. Des.*, 2022, **224**, p 111350.
4. M. Mudasser Khan, K. Mairaj Deen, and W. Haider, Combinatorial Development and Assessment of a Zr-Based Metallic Glass for Prospective Biomedical Applications, *J. Non Cryst. Solids*, 2019, **523**, p 119544.
5. V.S. Vasantha, H.-S. Chin, and E. Fleury, Corrosion properties of Ni-Nb & Ni-Nb-M (M = Zr, Mo, Ta & Pd) metallic glasses in simulated PEMFC conditions, *J. Phys. Conf. Ser.*, 2009, **144**, p 012008. <https://doi.org/10.1088/1742-6596/144/1/012008>

6. Z.F. Wu, Q.P. Cao, Y. Ma, C. Wang, S.Y. Liu, X. Qian, and J.Z. Jiang, Thickness-Dependent Pitting Corrosion Behavior in Ni-Nb thin Film Metallic Glass, *Thin Solid Films*, 2014, **564**, p 294–298.
7. S. Thanka Rajan and A. Arockiarajan, Thin Film Metallic Glasses for Bioimplants and Surgical Tools: A Review, *J. Alloys Compd.*, 2021, **876**, p 159939.
8. M. Naka, Corrosion Resistivity of amorphous Iron Alloys Containing Chromium, *J. Japan Inst. Metals*, 1974, **38**, p 835–841.
9. K. Hashimoto, WR Whitney Award Lecture: In Pursuit of New Corrosion-Resistant Alloys, *Corrosion*, 2002, **58**(09), p 715.
10. M. Adamzadeh, M.H. Enayati, and M. Shamanian, Ni-Nb Amorphous Coatings Prepared by Mechanical Alloying Method, *J. Non Cryst. Solids*, 2020, **547**, p 120311. <https://doi.org/10.1016/j.jnoncrysol.2020.120311>
11. A.P. Wang, X.C. Chang, W.L. Hou, and J.Q. Wang, Preparation and Corrosion Behavior of Amorphous Ni-Based Alloy Coatings, *Mater. Sci. Eng. A*, 2007, **449**, p 277–280.
12. J. Plummer, Tunable Nanostructures, *Nat. Mater.*, 2015, **14**(6), p 556–556.
13. A. Inoue and N. Nishiyama, New Bulk Metallic Glasses for Applications as Magnetic-Sensing, Chemical, and Structural Materials, *MRS Bull.*, 2007, **32**(8), p 651–658.
14. W. Lu, J. Tseng, A. Feng, and J. Shen, Structural Origin of the Enhancement in Glass-Forming Ability of Binary Ni-Nb Metallic Glasses, *J. Non Cryst. Solids*, 2021, **564**, p 120834.
15. L. Xia, W.H. Li, S.S. Fang, B.C. Wei, and Y.D. Dong, Binary Ni-Nb Bulk Metallic Glasses, *J. Appl. Phys.*, 2006, **99**(2), p 026103.
16. Z. Zhu, H. Zhang, D. Pan, W. Sun, and Z. Hu, Fabrication of Binary Ni-Nb Bulk Metallic Glass With High Strength and Compressive Plasticity, *Adv. Eng. Mater.*, 2006, **8**(10), p 953–957.
17. A. Espinoza, A. Soriano, I.A. Figueroa, and F.J. Rodríguez, Effect of the pH on the Corrosion Behavior for a Binary Metallic Glass, *ECS Trans.*, 2020, **106**, p 63.
18. Z.M. Wang, J. Zhang, and J.Q. Wang, Pit Growth in a Ni-Nb Metallic Glass Compared with its Crystalline Counterpart, *Intermetallics*, 2010, **18**(11), p 2077–2082.
19. K. Tamilselvam, J. Singh Saini, D. Xu, and D. Brabazon, Corrosion Behavior of New Rare-Earth Free Cu-Based Metallic Glasses in NaCl Solution of Different Molarity, *J. Mater. Res. Technol.*, 2022, **16**, p 482–494.
20. C. Afonso, K. Martínez, V. Amigó, C.A. Dell, J.E. Spinellia, and C.S. Kiminamia, Characterization, Corrosion Resistance and Hardness of Rapidly Solidified Ni-Nb Alloys, *J. Alloys Compd.*, 2020, **829**, p 154529. <https://doi.org/10.1016/j.jallcom.2020.154529>
21. A. Igual Muñoz and S. Mischler, Interactive Effects of Albumin and Phosphate Ions on the Corrosion of CoCrMo Implant Alloy, *J. Electrochem. Soc.*, 2007, **154**10, p 562. <https://doi.org/10.1149/1.2764238>
22. Q. Liu, B. Zhou, J. Zhang, W. Zhang, M. Zhao, N. Li, M. Xiong, J. Chen, Y. Yu, and S.Y. Song, Influence of Ru-Ni-Nb Combined Cathode Modification on Corrosion Behavior and Passive Film Characteristics of Ti-6Al-4V Alloy used for Oil Country Tubular Goods, *Corros. Sci.*, 2022, **207**, p 110569.
23. H. Liao, M. Wu, D. Deng, W. Zhong, B. Xiong, and Y. Tong, Effects of Ti Content on the Microstructure, Mechanical Properties and Corrosion Behavior of Ti_xZrNb Alloys, *J. Mater. Sci. Technol.*, 2022, **19**, p 1433–1443.
24. K. Zhao, N. Wang, S. Li, G. Zhou, X. Teng, J. Xu, Y. Wang, and J. Li, Corrosion Behavior of Ni₆₂Nb₃₃Zr₅ Bulk Metallic Glasses After Annealing and Cryogenic Treatments, *Chem. Phys. Mater.*, 2023, **2**, p 58–68.
25. D.C. Harris, *Quantitative chemical analysis*, 4th ed. W. H. Freeman and Company, USA, 1995
26. L. Jiang, Z.Q. Chen, H.B. Luf, H.B. Kec, Y. Yuana, Y.M. Donga, and X.K. Meng, Corrosion Protection of NiNb Metallic Glass Coatings for 316SS by Magnetron Sputtering, *J. Mater. Sci. Technol.*, 2021, **79**, p 88–98.
27. J. Gu, S. Lu, Y. Shao, and K. Yao, Segregating the Homogeneous Passive Film and Understanding the Passivation Mechanism of Ti-Based Metallic Glasses, *Corros. Sci.*, 2021, **178**, p 109078.
28. A.W.E. Hodgson, S. Kurz, S. Virtanen, V. Fervel, C.-O.A. Olsson, and S. Mischler, Passive and Transpassive Behaviour of CoCrMo in Simulated Biological Solutions, *Electrochim. Acta*, 2004, **49**, p 2167–2178. <https://doi.org/10.1016/j.electacta.2003.12.043>
29. M.G. Fontana and N.D. Greene, *Corrosion engineering*, 2nd ed. Mc Graw Hill International, Tokyo, 1978
30. C. Qiao, M. Wang, L. Hao, X. Jiang, X. Liu, C. Thee, and X. An, In-situ EIS Study on the Initial Corrosion Evolution Behavior of SAC305 Solder Alloy Covered with NaCl Solution, *J. Alloys Compd.*, 2020, **852**, p 156953. <https://doi.org/10.1016/j.jallcom.2020.156953>
31. P.C. Karulkar, Effects of Sputtering on the Surface Composition of Niobium Oxides, *J. Vac. Sci. Technol.*, 1981, **18**, p 169. <https://doi.org/10.1116/1.570717>
32. M. Grundner and J. Halbritter, On the Natural Nb₂O₅ Growth on Nb at Room Temperature, *J. Surf. Sci.*, 1984, **136**, p 144–154. [https://doi.org/10.1016/0039-6028\(84\)90661-7](https://doi.org/10.1016/0039-6028(84)90661-7)
33. On. Halbritter, The Oxidation and on the Superconductivity of Niobium, *J. Appl. Phys. A*, 1987, **43**, p 1–28. <https://doi.org/10.1007/BF00615201>
34. A.N. Mansour, Characterization of NiO by XPS, *Surf. Sci. Spectra*, 1994, **3**, p 231–239. <https://doi.org/10.1116/1.1247751>
35. P. Salunkhe, Investigation on Tailoring Physical Properties of Nickel Oxide Thin Films Grown by DC Magnetron Sputtering, *Mater. Res. Express*, 2020, **7**, p 016427. <https://doi.org/10.1088/2053-1591/ab69c5>
36. M.A. Peck and M.A. Langell, Comparison of Nanoscaled and Bulk NiO Structural and Environmental Characteristics by XRD, XAFS, and XPS, *Chem. Mater.*, 2012, **24**(23), p 4483–4490. <https://doi.org/10.1021/cm300739y>
37. J. Jayaraj, D. Nanda Gopala Krishna, and U. Kamachi Mudali, Passive Film Properties and Corrosion Behavior of Ni-Nb and Ni-Nb-Ta Amorphous Ribbons in Nitric Acid and Fluorinated Nitric Acid Environments, *Mat. Chem. Phys.*, 2015, **151**, p 318–329.
38. G. Jiang, L. Liu, D. Xu, Y. Li, W. Kuang, and M. Wang, Waterside Corrosion of M5 Alloy in Lithiated/Borated and Supercritical Water: Influences of Aqueous Environments, *J. Supercrit. Fluids*, 2023, **193**, p 105828.
39. G. Jiang, D. Xu, L. Liu, X. Ding, W. Kuang, and M. Wang, Oxidation of typical Zr-1 Nb alloy in high-temperature air under 700-900 °C, *Corros. Sci.*, 2022, **209**, p 110701.
40. G. Jiang, D. Xu, W. Yang, L. Liu, Y. Zhi, and J. Yang, High-Temperature Corrosion of Zr-Nb Alloy for Nuclear Structural Materials, *Prog. Nucl. Energy*, 2022, **154**, p 104490.

Publisher's Note Springer Nature remains neutral with regard to jurisdictional claims in published maps and institutional affiliations.

Springer Nature or its licensor (e.g. a society or other partner) holds exclusive rights to this article under a publishing agreement with the author(s) or other rightsholder(s); author self-archiving of the accepted manuscript version of this article is solely governed by the terms of such publishing agreement and applicable law.